DEVELOPMENT OF A 3-D UNSTRUCTURED GRID SIMULATION CAPABILITY FOR TURBULENT AEROSPACE FLOWS

Bigarella, E.D.V. , Moreira, F.C. , Azevedo, J.L.F.
*Instituto Tecnológico de Aeronáutica, CTA – São José dos Campos – SP – BRAZIL, **Instituto de Aeronáutica e Espaço, CTA – São José dos Campos – SP – BRAZIL, ***Instituto de Aeronáutica e Espaço, CTA – São José dos Campos – SP – BRAZIL

Keywords: *CFD, Unstructured grids, Turbulent flows, Aerospace applications*

Abstract

The Computational Fluid Dynamics group at Instituto de Aeronáutica e Espaço has been working, for some time now, on the development of numerical simulation capabilities that can handle the actual launch vehicle configurations of interest at the institute. At this point along the development process, good results have been achieved with adaptive, unstructured grid, finite volume techniques for 3-D, inviscid and turbulent viscous flows over sounding rockets and satellite launcher configurations. Therefore, the main purpose of the present work is to describe the capability currently available at the institute for flow simulation over such realistically complex aerospace geometries. The paper briefly describes the theoretical and numerical formulations and it concentrates on the aerodynamic analysis of the configurations of interest in order to demonstrate the available capabilities.

1 Introduction

Many approaches are available in the literature to simulate aerodynamic flows over 3-D aerospace configurations. The CFD group at Instituto de Aeronáutica e Espaço (IAE) has already achieved good results using finite difference techniques on structured grids. This paper discusses the results obtained using a finite volume method on 3-D unstructured meshes to simulate turbulent viscous
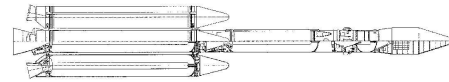

Fig. 1 VLS geometry overview.

flows over typical aerospace configurations. One of such aerospace configurations of interest at IAE is the first Brazilian Satellite Launch Vehicle (VLS). The VLS launcher is composed by a central body and four strap-on boosters. An illustrative sketch of the rocket is presented in Fig. 1.

The computational code solves the Reynolds-averaged Navier-Stokes (RANS) equations. A fully explicit, 2nd-order accurate, 5-stage, Runge-Kutta time stepping scheme is used to perform the time marching of the flow equations. For flux calculations on volume faces, either a Jameson centered scheme [1] plus explicitly added artificial dissipation terms, or a Roe flux-difference splitting scheme [2] can be used. Boundary conditions are set through the use of ghost cells attached to the boundary faces. The implementation uses a cell-centered, face-based data structure and the code can use meshes with any combination of tetrahedra, hexahedra, triangular-base prisms and pyramids. Extensive validation of this method had already been initiated and one is referred to [3] for a careful analysis of the initial validation results.

Advanced eddy-viscosity turbulence models are also available in order to include turbulence effects into the RANS equations. Viscous simulations at high Reynolds number are typical for aerospace applications, such as the ones of interest at IAE. Numerical simulations of such flight conditions which neglect turbulence effects do not have any physical meaning and, therefore, have limited practical application. In order to obtain useful viscous simulation results, the Spalart-Allmaras one-equation [4] and the SST two-equation [5] turbulence models are used. These models are suitable for external aerodynamics applications and they can predict flow separation with acceptable levels of accuracy. The CFD group at IAE has already some previous experience with such closures for turbulent flow simulations [6, 7, 8].

A full multigrid (FMG) scheme is also available in order to achieve better convergence rates for the simulations. To build the mesh sequence for the multigrid procedure, an agglomeration scheme based on cell or node seeds is used. A robust and consistent method for 3-D turbulent flow simulations has been derived and included into the present numerical formulation. This methodology allows for successful simulations of high-Reynolds number turbulent flows at very acceptable computational efforts.

Simulation results obtained with the present code for the VLS configuration as well as other typical aerospace test cases are discussed in this paper. Turbulent transonic and supersonic flows are simulated. The numerical results obtained so far show good agreement with the experimental data [9] and they represent all the relevant aerodynamic features observed in experimental tests.

2 Theoretical Formulation

The flows of interest for the present CFD group are modeled by the 3-D compressible Reynolds-averaged Navier-Stokes (RANS) equations. These equations can be written in dimensionless form, assuming a perfect gas, as

$$\frac{\partial Q}{\partial t} + \nabla \vec{P}_e = \nabla \vec{P}_v \,, \quad \vec{P} = E\,\hat{\imath}_x + F\,\hat{\imath}_y + G\,\hat{\imath}_z \,, \quad (1)$$

where Q is the dimensionless vector of conserved variables, defined as

$$Q = \begin{bmatrix} \rho & \rho u & \rho v & \rho w & e \end{bmatrix}^{\mathrm{T}} . \quad (2)$$

Here, ρ is the fluid density, u, v and w are the Cartesian velocity components and e is the fluid total energy per unit of volume. The formulation for the dimensionless inviscid flux vectors, E_e, F_e and G_e, and the dimensionless viscous flux vectors E_v, F_v and G_v, as well as other definitions in Eq. (1) can be found in [8].

The main interest of the present CFD group is on high-Reynolds number simulations of flows over complex aerodynamic configurations. Such applications require adequate turbulence closures in order to correctly account for the large transport effects of the turbulence at such flight conditions. Two turbulence closures have been chosen in the present context, namely, the Spalart-Allmaras [4] (SA) one-equation model and the Menter SST [5] two-equation model. Both closures are particularly suited for aerodynamic flow simulations and separation prediction [5]. Furthermore, they are also less restrictive in relation to the grid refinement near the wall than other two-equation closures such as the $k - \varepsilon$ family of models [5]. Implementation details on this formulation and other numerical results can be found in [3] and [10].

3 Numerical Formulation

The finite volume method is used to obtain the solution of the RANS equations. The formulation of the method is obtained by an integration of the flow equations in a finite volume. The application of the Gauss theorem for each finite volume yields, for an elementary volume and assuming a stationary mesh

$$\frac{\partial Q_i}{\partial t} = -\frac{1}{V_i} \sum_{k=1}^{nf} \left[\vec{P}_{e_k} - \vec{P}_{v_k} \right] \cdot \vec{S}_k \,, \quad (3)$$

where nf is the number of faces which form the i-th control volume and $\vec{S}_k$ is the outward oriented normal area vector of the k-th face. The discrete value of the vector of conserved variables for the

i-th control volume is defined as the mean value of the conserved variables in the volume. The code is able to simulate flows on grids comprised of tetrahedra, hexahedra, triangular-base prisms, pyramids or a mix of these types of elements. The previous equation also indicates that the integral was discretized assuming the fluxes to be constant on the faces.

4   Time Integration and Multigrid

Time integration of Eq. (3) is performed using a Runge-Kutta type scheme similar to the one proposed in [1]. In the present work, a 2nd-order accurate, 5-stage Runge-Kutta scheme is used. The time step for each volume is calculated assuming a constant CFL number throughout the computational domain. More details on this formulation can be found in [3] and [8].

A multigrid scheme is also available in the present numerical code in order to accelerate convergence to steady-state. The chosen multigrid algorithm is of a full approximation storage (FAS) type, which is the recommended method for nonlinear problems [11]. This method is based on exchanging both solution and residue values between different grid levels. It also relies on a good time marching procedure to be effective. This method has been successfully validated within the present 3-D unstructured computational code for inviscid to turbulent viscous simulations, as shown in [10]. In order to improve the multigrid algorithm as well as the computational method, the simulations start at the coarsest grid level. Some iterations with the Runge-Kutta time stepping are performed at this grid and a high-order interpolation is performed to the next finer grid. Some multigrid cycles are, then, performed to improve the solution at this grid. This procedure is repeated successively until the finest grid is reached, with a good initial guess to the solution. Multigrid cycles are, then, performed on the finest mesh until convergence is reached. This technique is usually denoted as full multigrid (FMG) method.

The coarse mesh levels used by the multigrid scheme are generated with an agglomeration technique. More details on the multigrid algorithm as well as the agglomeration technique can be found in [8].

5   Spatial Discretization

Both centered and upwind schemes are available in the present numerical method for computation of convective fluxes. Viscous fluxes are always computed by a second-order accurate centered scheme in the present paper.

5.1   Centered Scheme

The centered scheme used in this work for spatial discretization of the convective fluxes was proposed in [1]. For this scheme, the convective operator, CO_i, is calculated as the sum of the inviscid fluxes on the faces of the *i*-th volume

$$CO_i = \sum_{k=1}^{nf} \vec{P}_e(Q_k) \cdot \vec{S}_k \,, \quad Q_k = \frac{1}{2}(Q_i + Q_m). \quad (4)$$

In this expression, Q_i and Q_m are the conserved properties in the volumes at each side of the *k*-th face and *m* indicates the neighbor of the *i*-th element.

Centered schemes require the explicit addition of artificial dissipation terms in order to control nonlinear instabilities that may arise in the flow simulation. The artificial dissipation operator is built by a switch of undivided Laplacian and bi-harmonic operators [12]. In regions of high property gradients, the bi-harmonic operator is turned off in order to avoid oscillations. In smooth regions, the undivided Laplacian operator is turned off in order to maintain 2nd order accuracy. A numerical pressure sensor is responsible for this switching between the operators. The expression for the artificial dissipation operator as well as other details on the implementation can be found in [8].

5.2   Upwind   Flux-Difference   Splitting   Scheme

The upwind discretization in the present context is performed by the Roe flux-difference splitting

method [2]. For this scheme, the numerical flux for the *x*-direction, in the *k*-th face, can be written as

$$\overline{E}_{ek} = \frac{1}{2}\left[E_{e_L} + E_{e_R} - \left|\widetilde{A}\right|(Q_L - Q_R)\right] . \quad (5)$$

which results in

$$CO_i = \sum_{k=1}^{nf}\left(\overline{E}_{ek}\hat{\imath}_x + \overline{F}_{ek}\hat{\imath}_y + \overline{G}_{ek}\hat{\imath}_z\right)\cdot\vec{S}_k . \quad (6)$$

It can be shown that

$$\left|\widetilde{A}\right|(Q_R - Q_L) = \sum_\ell|\lambda_\ell|\,\alpha_\ell r_\ell , \quad (7)$$

where λ_ℓ is the ℓ-th eigenvalue related to the Euler equations, r_ℓ is the corresponding eigenvector and α_ℓ is the projection of the property jump at the interface over vector r_ℓ. Properties in the volume faces are computed using the Roe average procedure, as detailed in [2]. The cited reference also presents the definitions for the r_ℓ and α_ℓ terms in the previous formulation.

To achieve 2nd order accuracy in space for the Roe scheme, linear distributions of properties are assumed at each cell to compute the left and right states in the face. Such states are represented by the *L* and *R* subscripts, respectively, in the previous Roe definitions.

The linear reconstruction of properties is achieved through a MUSCL [13] scheme, in which the property at the interface is obtained through a limited extrapolation using the cell properties and their gradients. The expressions for the reconstructed properties in the control volume faces can be written as

$$q = q_i + \psi\nabla q_i \cdot \vec{r}_i , \quad (8)$$

where ∇q_i is the gradient computed for the *i*-th cell; ψ represents the limiter; and $\vec{r}_i$ is the distance vectors from the *i*-th cell centroid to the face centroid.

The *minmod* limiter [14] is used in the present context. The extension of the 1-D limiter, as defined in [14], to the 3-D case is based on [15] and [16]. For each *n*-th vertex of the *i*-th cell, the

property $q_{in} = q(x_n, y_n, z_n)$ in that vertex is reconstructed as

$$q_{in} = q_i + \nabla q_i \cdot \vec{r}_n , \quad (9)$$

where $\vec{r}_n$ is the distance of the *n*-th vertex of the *i*-th cell to the centroid of this cell. A limiter is computed at each vertex of the control volume. The limiter value for the *i*-th control volume is finally obtained as the minimum of the limiters computed at the vertexes.

5.3 Viscous Flux Computation

The Navier-Stokes viscous terms are computed by a second-order accurate centered scheme. The viscous operator in the *i*-th control volume is calculated as the sum of the viscous fluxes on the faces which constitute the volume. In this case, both the conserved variable vector and the derivatives on the face, used to compute the viscous terms, are calculated as the arithmetic average between these quantities in the two volumes which contain the face. Derivatives of flow variables, for each control volume, are calculated in the standard finite volume approach in which these derivatives are transformed, by the gradient theorem, into surface integrals around the control volume [17, 18].

6 Adaptive Mesh Refinement

The quality of numerical simulations is extremely dependent on the mesh. For high quality solutions, it is usually necessary to concentrate points in regions where the flow presents sudden variations. The idea behind the adaptive mesh refinement (AMR) is to attribute to the flow the responsibility of concentrating computational points by using numerical sensors and automatic routines that alter the mesh. The mesh concentration in such regions can be incremented by many forms. One way is to locally add more points, which is the chosen option in the present context due to its ease of implementation in an unstructured grid context. The sensor for regions that need refinement uses an undivided density gradient [19], normalized by the largest difference

in density verified in the flow. If the sensor in a given cell is greater than a threshold value, the volume is refined [3].

Each type of element that the code can handle is divided differently. A tetrahedron is divided in 8 tetrahedra; a hexahedron is divided in 8 hexahedra; a triangular base prism is divided in 8 triangular-base prisms; and a square-base pyramid is divided in 6 square-base pyramids and 4 tetrahedra. The present AMR procedure does not allow twice refined elements to neighbor other non-refined cells. This procedure guarantees smoother transitions of element sizes throughout the mesh. It is also important to remark here that such approach allows for the creation of hanging nodes in the refined mesh. Nevertheless, the data structure of the code is face-based, which means that it is irrelevant if the node is a hanging node or not. Furthermore, all loops are face-based and this makes the flux and dissipation term calculations independent of the type of element.

7 Results and Discussion

In order to evaluate the code, aerodynamic flows over various configurations are simulated. Inviscid supersonic flows about the VLS are considered for the adaptive mesh refinement assessment. Flat plate flows are used to address the turbulent flow simulation capability. Additionally, turbulent viscous flows over the VLS central body are simulated for various angles of attack. All results are compared to available experimental and/or theoretical data in order to address the the numerical tool. The multigrid capability has been used in the simulations to accelerate convergence to steady-state solutions.

7.1 Flat Plate Turbulent Flow

Zero-pressure gradient flat plate low speed flows are considered for Reynolds number $Re = 1$ million and freestream Mach number $M_\infty = 0.3$. Simulations with both SA and SST turbulence models are included in order to provide some comparison of the results for both closures. Fig-
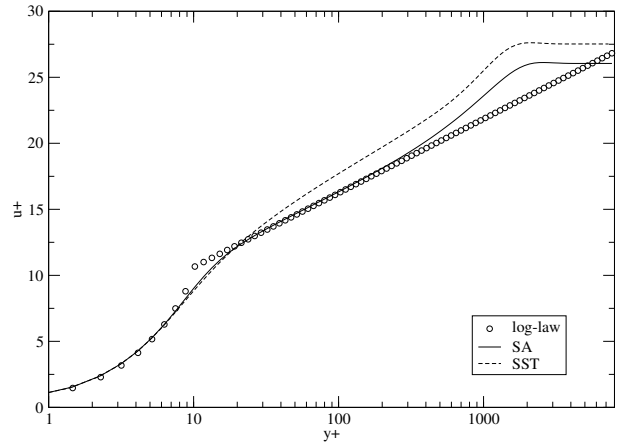

Fig. 2 Comparative results between numerical and theoretical boundary layer profiles.

ure 2 shows the turbulent numerical boundary layers compared to the theoretical log-law solution [20]. One can clearly observe in Fig. 2 a strikingly coherence with the theoretical curve in the case of the SA turbulence model. In the case of the SST two-equation model, the coherence between both results is not as good in the inertial part of the boundary layer. A very similar behavior of the SST closure in this test case has been observed in a finite-difference context, as one can verify in [7]. This may be indicative of some issues concerning the formulation provided in the articles available to the authors to guide the model implementation, especially regarding the model constants. Due to better numerical results and lower computational cost, the SA model has been chosen for the forthcoming simulations.

7.2 VLS Turbulent Supersonic Flows

The turbulent flow at $M_\infty = 2.0$, $Re = 30$ million and zero angle of attack over the VLS second stage flight configuration is simulated. The mesh used in this case has 201,565 nodes and 188,480 elements and it is clustered near the solid surface to guarantee good resolution of the turbulent velocity profile. Figure 3 presents the dimensionless pressure contours over the vehicle forebody for this case. The flow is characterized by a detached shock wave in front of the vehicle, an expansion on the first and second corners of the payload fairing and a shock wave at the end of
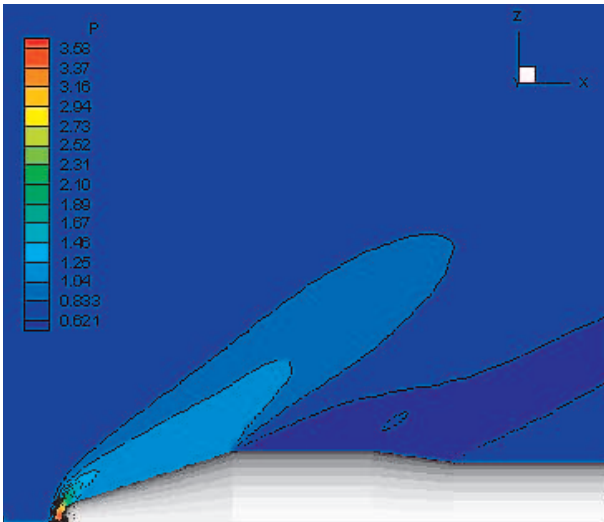
Fig. 3 Pressure contours over the VLS second stage flight configuration forebody for turbulent viscous flow simulations at $M_\infty = 2.0$, $Re = 30$ million and zero angle of attack.

the boattail. A comparison between the pressure coefficient distribution on the VLS surface for the turbulent numerical solution and experimental data is shown in Fig. 4. There are no relevant differences between the solutions for this case, as expected.

One of the objectives of the CFD group at IAE is to determine the stability derivatives of launch vehicles for many flow conditions. This is normally performed by the determination of the pressure coefficient on the vehicle wall for different angles of attack at the flow conditions of interest. Therefore, a simulation of the VLS flying at angle of attack different from zero is a relevant condition to be tested. As launch vehicles fly at very small angles of attack, the authors decided to simulate the flow over the VLS second stage flight configuration at $M_\infty = 2.0$, $\alpha = 2.0$ deg. and $Re = 30$ million, a condition with available experimental results. Figure 5 presents the Mach number contours over the VLS forebody. The detached shock wave is no longer symmetrical. The shock wave on the windside is stronger than that in the leeside because the deflection in the flow is larger. This can be seen as a larger region of lower Mach numbers in the windside. Furthermore, the boundary layer on the leeside is thicker
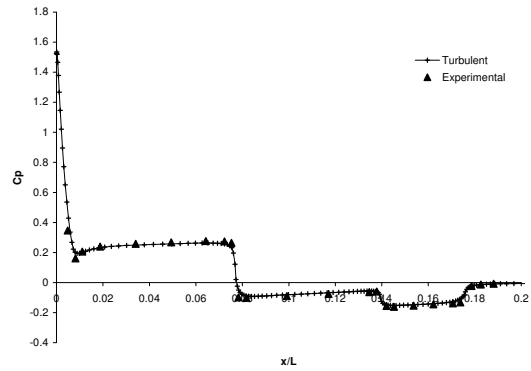

Fig. 4 Pressure coefficient distributions on the VLS second stage flight configuration forebody in the pitching plane at $M_\infty = 2.0$, $Re = 30$ million and zero angle of attack.

than on the windside. A comparison between numerical and experimental data for the pressure coefficient on the vehicle forebody is presented in Fig. 6. The numerical solution presents good agreement with the numerical data, as the main tendencies of the pressure coefficient distribution are numerically obtained.

7.3 VLS Turbulent Transonic Flows

A turbulent viscous flow over the VLS at $M_\infty = 0.9$, $Re = 25$ million and zero angle of attack is now considered. The mesh used in this case has 100,815 nodes and 89,280 elements. Figure 7 presents the Mach number contours over the vehicle forebody. This figure evidences the presence of the boundary layer over the vehicle. A stagnation point occurs in front of the vehicle. There is a supersonic expansion over the end of the conical forebody. This causes the formation of a supersonic region on the payload cylinder which is ended by a shock wave. Due to the boundary layer, this shock wave does not reach the body. The region over the end of the boattail presents very small velocities, but the boundary layer does not separate because of the turbulent characteristic of the flow. In fact, laminar simulations of this flow condition indicate boundary layer separation. A comparison between the pressure coefficient distribution on the VLS surface for the Euler and the turbulent numerical so-
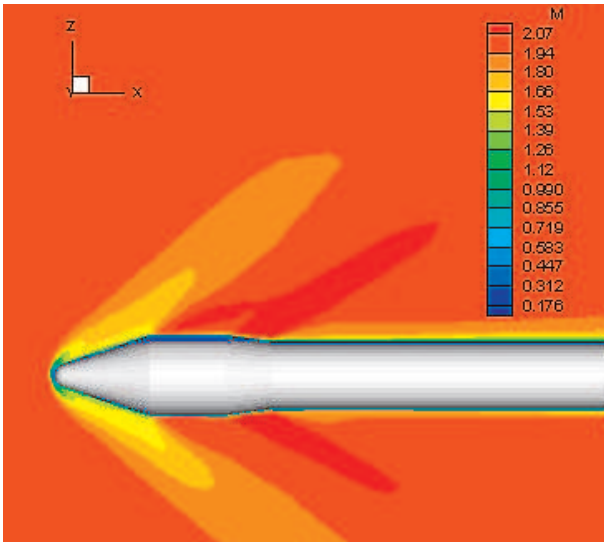
Fig. 5 Mach number contours over the VLS second stage flight configuration forebody for turbulent viscous flow simulations at $M_\infty = 2.0$, $Re = 30$ million and $\alpha = 2.0$ deg.

Fig. 6 Pressure coefficient distributions on the VLS second stage flight configuration forebody in the pitching plane for turbulent viscous flow simulations at $M_\infty = 2.0$, $Re = 30$ million and $\alpha = 2.0$ deg.

lutions is shown in Fig. 8, which also includes experimental data. The simulation considering turbulence effects performs more consistently if compared to the Euler simulation. A much better solution is obtained, which captures the shock wave over the payload fairing and which correctly predicts the position of the compression at the end of the boattail.

7.4 Adaptive Mesh Refinement Results

The results obtained in the simulation of supersonic inviscid flow over the complete vehicle clearly showed the need for more mesh refinement in the booster nose cap region and in the vehicle forebody [21]. The adaptive mesh refinement technique is applied on such cases in order to enhance the solution quality.

7.4.1 *Tetrahedral Mesh*

In this case, inviscid flow simulations over the VLS first stage flight configuration at $M_\infty = 2.0$ and zero angle of attack are considered. The 3-D computational grid is composed of tetrahedra. Because of memory limitations, the authors had to limit the simulation to only one mesh refinement pass, although the routines are able to
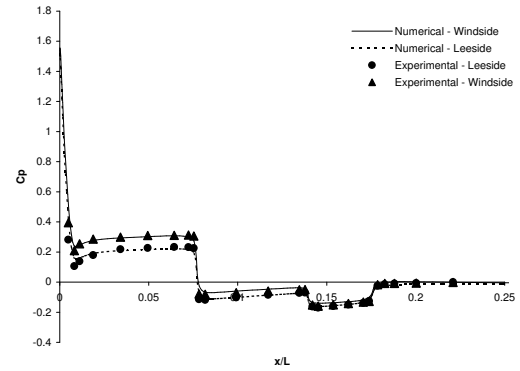
perform as many refinement passes as the user desires, and to limit the refinement threshold to 0.003. The adapted mesh has approximately 243,000 nodes and 1.1 million elements. Detailed views of the adapted mesh over the vehicle forebody and over the booster nose cap region are presented in Figs. 9 and 10. Clearly, the AMR procedure is able to detect the presence of the shock waves and expansions, and the mesh is subsequently refined in these regions.

7.4.2 *Hexahedral Mesh*

In order to test the capability of the refinement procedure to handle hexahedral and prismatic meshes, the inviscid flow over the VLS central body for $M_\infty = 2.0$ and zero angle of attack is considered. The original mesh used for the calculations is shown in Fig. 11, which presents a close view of the vehicle nose cap. The same view for the adapted mesh is presented in Fig. 12. The original mesh has 100,815 nodes and 89,280 volumes. The adapted mesh, after one refinement pass, has approximately 346,000 nodes and 286,000 elements. Again, the AMR procedure is able to determine the presence of shock waves and expansions and refine the mesh in the regions where these phenomena are detected. The threshold for the density gradient sensor used in this simulation is 0.09, which is bigger than the one
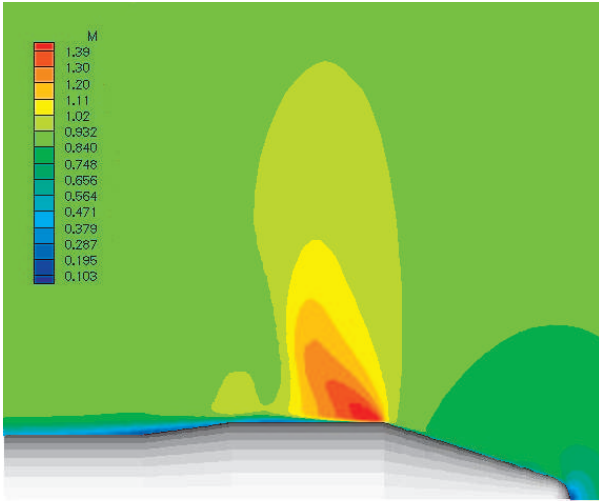
Fig. 7 Mach number contours over the VLS second stage flight configuration forebody for turbulent viscous flow simulations at $M_\infty = 0.9$, $Re = 25$ million and zero angle of attack.

Fig. 8 Pressure coefficient distributions on the VLS second stage flight configuration forebody in the pitching plane for turbulent viscous flow simulations at $M_\infty = 0.9$, $Re = 25$ million and zero angle of attack.

used in the case with a tetrahedral mesh. This comes from the fact that the sensor is based on gradient calculation, which depends on the size of the elements. The hexahedral mesh is more refined near the body than the tetrahedral mesh, causing the gradients calculated in the hexahedral mesh to be bigger than the ones calculated in the tetrahedral mesh. Therefore, in order to have mesh refinement in regions of the hexahedral meshes similar to that obtained using the tetrahedral mesh, a larger value for the threshold value should be used.

8 Concluding Remarks

The paper presents results obtained with a finite volume code developed to solve the RANS equations over aerospace configurations at Instituto de Aeronáutica e Espaço. The code uses an explicit Runge-Kutta type scheme to perform the time marching of the governing equations. Convective fluxes on the volume faces are computed by either a centered scheme plus explicitly added artificial dissipation terms or a flux-difference splitting upwind scheme. The code structure is of a cell-centered and face-based type, and it is designed to use unstructured meshes composed by any combination of tetrahedra, hexahedra, prisms
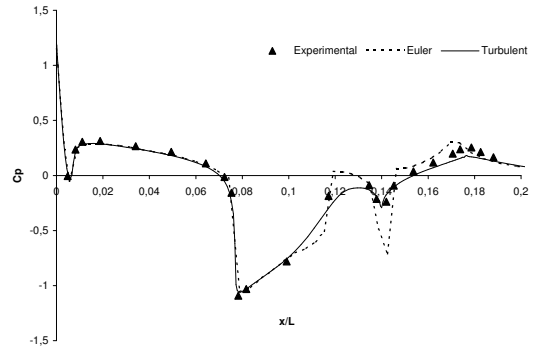
and pyramids. An adaptive mesh refinement capability is also included in the numerical tool in order to improve the numerical solution quality.

Turbulence effects are added to the RANS formulation by eddy-viscosity type turbulence models. The Spalart-Allmaras single-equation and the SST two-equation turbulence closures are chosen in order to include such turbulence effects. The comparison of the numerical boundary layers for a zero-pressure gradient flat plate flow with the corresponding theoretical log-law solution shows the level of accuracy that can be obtained with the present formulation. Furthermore, the code is also able to correctly solve for more complex flows, such as transonic or supersonic turbulent flows about typical aerospace configurations. Again, good approximation between experimental and numerical results could be obtained for such cases.

The results obtained using the adaptive mesh refinement capability show that such technique allows better representation of flow discontinuities within the computational domain. The procedure is able to detect regions which need more mesh refinement, such as shock waves and expansions. Such aerodynamic phenomena are easily detected by a sensor based on density gradients computed at each control volume throughout the computational domain. In every simulation of
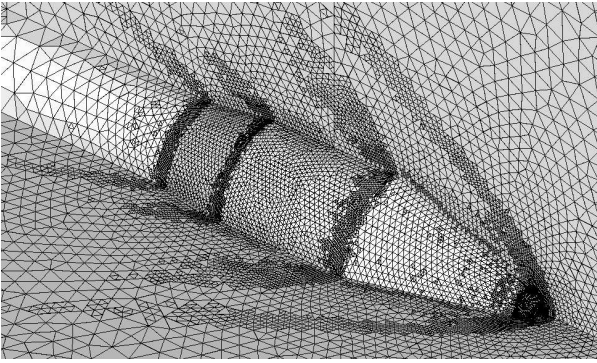
Fig. 9 Detailed view of the adapted mesh near the central body forebody.
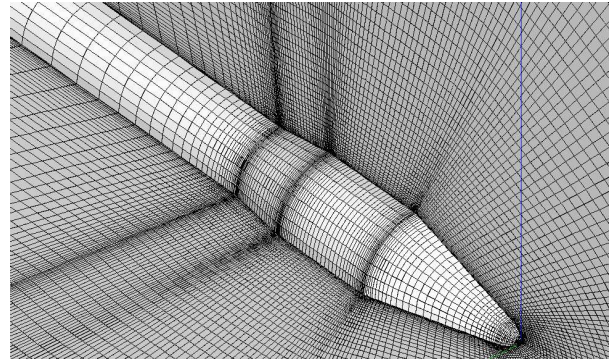

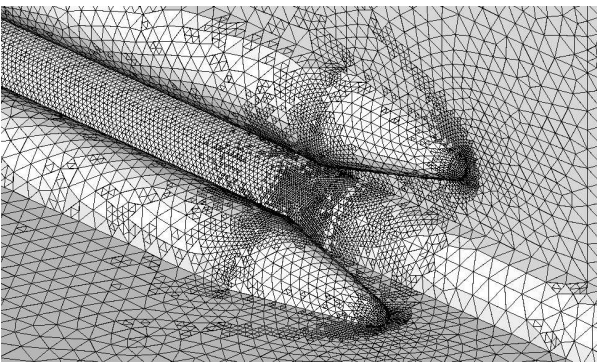**Fig. 11** Detailed view of the original mesh near the central body forebody.

Fig. 10 Detailed view of the adapted mesh near the booster nose cap.
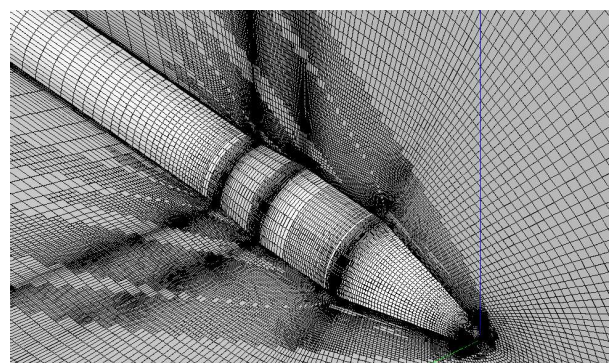

Fig. 12 Detailed view of the adapted mesh near the central body forebody.

flows about the VLS configuration, crisper shock waves and more correct expansions are observed in the results due to the use of the adaptive mesh refinement procedure.

Finally, the agglomeration multigrid scheme provides a large convergence acceleration for the numerical simulations. In a general manner, numerical solutions of complex flows such as supersonic turbulent flows about typical aerospace configurations can be obtained in half the previous time used by the single-grid simulation. The results presented here are a good indication of the capability of simulating turbulent flows about realistic aerospace configurations that has been developed by the CFD group at IAE.

9 Acknowledgments

References

[1] Jameson, A., Schmidt, W., and Turkel, E., "Numerical Solution of the Euler Equations by Finite Volume Methods Using Runge-Kutta Time-Stepping Schemes," *Proceedings of the AIAA 14th Fluid and Plasma Dynamics Conference*, AIAA Paper No. 81-1259, Palo Alto, CA, 1981.

[2] Roe, P. L., "Approximate Riemann Solvers, Parameter Vectors, and Difference Schemes," *Journal of Computational Physics*, Vol. 43, No. 2, 1981, pp. 357–372.

[3] Scalabrin, L. C., *Numerical Simulation of Three-Dimensional Flows over Aerospace Configurations*, Master's thesis, Instituto Tecnológico de Aeronáutica, São José dos Campos, SP, Brazil, 2002.

[4] Spalart, P. R. and Allmaras, S. R., "A One-Equation Turbulence Model for Aerodynamic Flows," *30th AIAA Aerospace Sciences Meeting and Exhibit*, AIAA Paper No. 92-0439, Reno, NV, Jan. 1992.

[5] Menter, F. R. and Grotjans, H., "Application of Advanced Turbulence Models to Complex Industrial Flows," *Second International Conference on Advances in Fluid Mechanics*, Udine, Italy, May 1998.

[6] Strauss, D. and Azevedo, J. L. F., "Unstructured Multigrid Simulation of Turbulent Launch Vehicle Flows Including a Propulsive Jet," *Proceedings of the 20th AIAA Applied Aerodynamics Conference*, AIAA Paper No. 2002-2720, St. Louis, MO, June 2002.

[7] Bigarella, E. D. V., *Three-Dimensional Turbulent Flow Simulations over Aerospace Configurations*, Master's thesis, Instituto Tecnológico de Aeronáutica, São José dos Campos, SP, Brazil, 2002.

[8] Bigarella, E. D. V., Basso, E., and Azevedo, J. L. F., "Centered and Upwind Multigrid Turbulent Flow Simulations with Applications to Launch Vehicles," *22nd AIAA Applied Aerodynamics Conference and Exhibit*, AIAA Paper No. 2004-5384, Providence, RI, Aug. 2004, (to appear).

[9] Moraes, P., Jr., and Augusto Neto, A., "Aerodynamic Experimental Investigation of the Brazilian Satellite Launch Vehicle (VLS)," *Proceedings of the 3rd Brazilian Thermal Sciences Meeting – ENCIT 90*, Vol. 1, Itapema, SC, Brazil, Dec. 1990, pp. 211–215.

[10] Bigarella, E. D. V., Basso, E., and Azevedo, J. L. F., "Multigrid Adaptive-Mesh Turbulent Simulations of Launch Vehicle Flows," *Proceedings of the 21st AIAA Applied Aerodynamics Conference*, AIAA Paper No. 2003-4076, Orlando, FL, USA, June 2003.

[11] Fletcher, C. A. J., *Computational Techniques for Fluid Dynamics 2. Specific Techniques for Different Flow Categories*, chap. 6, Springer-Verlag, 1988, pp. 203–209.

[12] Mavriplis, D. J., "Accurate Multigrid Solution of the Euler Equations on Unstructured and Adaptive Meshes," *AIAA Journal*, Vol. 28, No. 2, Feb. 1990, pp. 213–221.

[13] van Leer, B., "Towards the Ultimate Conservative Difference Scheme. V. A Second-Order Sequel to Godunov's Method," *Journal of Computational Physics*, Vol. 32, 1979, pp. 101–136.

[14] Hirsch, C., *Numerical Computation of Internal and External Flows Volume 2: Computational Methods for Inviscid and Viscous Flows*, Wiley, Chichester, 1991.

[15] Barth, T. J. and Jespersen, D. C., "The Design and Application of Upwind Schemes on Unstructured Meshes," *27th AIAA Aerospace Sciences Meeting*, AIAA Paper No. 89-0366, Reno, NV, Jan. 1989.

[16] Azevedo, J. L. F., Figueira da Silva, L. F., and Strauss, D., "Order of Accuracy Study of Unstructured Grid Finite Volume Upwind Scheme," Paper submitted to the *Int. J. Numer. Meth. Fluids*, 2001.

[17] Swanson, R. C. and Radespiel, R., "Cell Centered and Cell Vertex Multigrid Schemes for the Navier-Stokes Equations," *AIAA Journal*, Vol. 29, No. 5, May 1991, pp. 697–703.

[18] Azevedo, J. L. F., Strauss, D., and Figueira da Silva, L. F., "An Order of Accuracy Analysis for Flux-Vector Splitting Schemes on Unstructured Grids," *Proceedings of the 15th Brazilian Congress of Mechanical Engineering - COBEM 99*, Águas de Lindóia, SP, Brazil, Nov. 1999.

[19] Azevedo, J. L. F. and Korzenowski, H., "Comparison of Unstructured Grid Finite Volume Methods for Cold Gas Hypersonic Flow Simulations," *Proceedings of the 16th AIAA Applied Aerodynamics Conference*, AIAA Paper No. 98-2629, Albuquerque, NM, June 1998.

[20] Tennekes, H. and Lumley, J. L., *A First Course in Turbulence*, The MIT Press, Cambridge, MA, USA, 1972.

[21] Scalabrin, L. C. and Azevedo, J. L. F., "Hierarchical Mesh Refinement and Coarsening for Unstructured Finite Volume Flow Simulations," *Proceedings of the 5th World Congress on Computational Mechanics*, Vienna, Austria, July 2002.